STABILITY OPTIMIZATION OF POWER ELECTRONIC EQUIPMENT BASED ON IMPROVED INERTIAL WEIGHT PARTICLE SWARM OPTIMIZATION

Hui YIN[1]

Power electronic devices have gradually become the core components of modern energy systems. However, due to their nonlinear dynamic characteristics and high-frequency switching characteristics, stability issues have seriously affected the operational safety of the system. Therefore, a stability optimization method for power electronic equipment based on Improved Inertial Weight Particle Swarm Optimization (IIW-PSO) is proposed. This method utilizes the IIW-PSO to optimize controller parameters, thereby reducing dependence on accurate mathematical models, and combines active damping compensation to adjust damping strength in real time. The voltage tracking error was the lowest at 1.25%, and the Total Harmonic Distortion (THD) was the lowest at 3.3%. In the practical application of stability testing for power electronic equipment, the voltage surge of the improved power electronic equipment system was only 2.9%, the highest steady-state error was only 2.1, and the maximum dynamic disturbance of the output voltage was 20V. The stability method based on the IIW-PSO has excellent anti-interference performance, can meet the high-performance and high reliability requirements, and further promote the development of power electronic equipment towards intelligence and high adaptability.

Keywords: Improved inertial weight particle swarm optimization; Power electronic equipment; Controller parameters; Active damping compensation; Stability

1. Introduction

With the transformation of global energy structure and the development of smart grids, power electronic devices have become the core components of modern energy systems, playing an important role in electric vehicles and renewable energy regeneration. The operation of these systems relies on power electronic converters [1]. However, the nonlinear dynamic characteristics of power electronic equipment, high-frequency switching operations, and parameter coupling problems under complex operating conditions have made the system vulnerable to stability issues such as voltage fluctuations, harmonic distortion, and transient currents [2]. Therefore, how to improve the dynamic stability and anti-interference ability of

[1]Assoc. Prof., School of Automotive Engineering, Xuzhou College of Industrial Technology, Xuzhou, 221000, China, e-mail: yinhuiyh6688@outlook.com

power electronic equipment has become a key focus for both academia and industry. In current research methods, Genetic Algorithm (GA) simulates the biological evolution to achieve global search, but their crossover and mutation operations have high computational costs and slow convergence speed. Although the Grey Wolf Optimization (GWO) has high optimization efficiency, it's likely to get stuck in local optima in high-dimensional parameter spaces [3]. The inertia weight Particle Swarm Optimization (PSO) has efficient controller parameter optimization capability and does not rely on precise mathematical models, which can balance the convergence speed and global optimality. Meanwhile, introducing active damping compensation can improve the dynamic adaptability of the control strategy to real-time disturbances [4-5]. Therefore, an improved PSO based on inertia weight and active damping compensation is built, and stability optimization of power electronic equipment is carried out based on the PSO. This study innovatively integrates the inertia weight PSO algorithm with active damping compensation, breaking through the efficiency and accuracy bottlenecks of traditional optimization methods.

The research is mainly conducted in four parts. The first part discusses the relevant research results of current electronic power equipment technology and particle swarm optimization algorithm. The second part is the design of a stability optimization method for power electronic equipment based on improved inertia weight particle swarm optimization. The third part analyzed the effectiveness of the research methods. The fourth part is a summary and discussion of the entire text.

2. Related work

Electronic power equipment has been widely used in various power systems and has received increasing research from scholars both domestically and internationally. Ma K et al. proposed a contour simulation technique for testing motor drive systems to address the difficulty of motors and drive converters to complex working conditions. The coupling degree of the drive converter was verified by testing the dynamometer and controller hardware. The results indicated that this method was applicable to task contour simulation [6]. Lyu H et al. proposed a fault current limiter to address the weak fault current tolerance in the distribution system of fully controlled power electronic devices. The suppression effect of various types of current limiters on fault current was summarized. The results indicated that this study provided a research foundation for adaptive fault current limiters [7]. Sun P et al. proposed a hybrid system consisting of multiple converters to address the unstable signals in power electronic devices such as renewable energy grid connected systems. The system consisted of a Virtual Synchronous Generator (VSG) system formed by the power grid and a Doubly Fed Induction Generator (DFIG). The system confirmed the correctness of interaction analysis [8]. Rivera S et al. proposed a charging infrastructure ecosystem to address the slow deployment.

This system covered charging technologies and structural configurations for different categories of electric vehicles. The results indicated that the system had a profound impact on the power grid [9]. Meng X et al. built a back-stepping control strategy relying on deep reinforcement learning to deal with the threat to the power supply stability of Dual Active Bridge (DAB) converters in power equipment. The compensation method based on deep reinforcement learning was taken to improve the operational efficiency. This method verified the effectiveness of the controller [10].

PSO algorithm is commonly used for optimizing optimal control parameters and has been explored. Pirozmand P. et al. proposed the PSO for task scheduling problems in cloud computing environments. During the process, multiple adaptive learning strategies were used to define ordinary particles and local optimal particles. The results indicated that this method could solve problems in a shorter time and obtain the best answer [11]. Otair M. et al. proposed a PSO algorithm combined with GWO to address the algorithm lacking recognition system attack attempts. This technology preserved individual best position information through PSO algorithm, preventing the GWO from getting stuck in local optima. The results indicated that the technology achieved necessary improvements in the grey wolf algorithm [12]. Zhang W et al. built a hierarchical PSO for the localization of unmanned aerial vehicles. This method introduced the reference optimal particle and search space reduction method and redesigned the particle update scheme. The results indicated that this method reduced both complexity and positioning error [13]. Tian J et al. designed a PSO relying on a variable proxy model to extend the multi-agent assisted evaluation algorithm. During the process, a variable model management strategy was adopted to accelerate the convergence speed. This technology provided efficiency in computing high-dimensional problems [14]. Lei Z et al. built a genetic learning-PSO based on chaotic local search for local optima in wind farm layout optimization. The parameters and search patterns of chaotic local search were analyzed. The results indicated that it performed excellently in terms of stability and robustness [15].

In summary, existing research has enabled various power electronic devices to be widely used, but there are still issues such as relying on accurate mathematical models and controller stability. The Improved Inertia Weight Particle Swarm Optimization (IIW-PSO) can optimize the controller parameters and overcome the shortcomings of traditional methods, such as high dependence on practical experience and low efficiency. Therefore, the stability optimization method for power electronic equipment based on IIW-PSO can optimize the efficiency of parameter tuning. It is expected to provide a more universal and efficient method in research.

3. Methods and materials

2.1. Design of controller parameter optimization method based on IIW-PSO

The penetration rate of electronic power equipment in various power systems has significantly increased. The stability of controllers for power electronic equipment generally needs to tune and optimize controller parameters. However, traditional algorithms have insufficient robustness and low computational efficiency. The study adopts an IIW-PSO, which dynamically adjusts the inertia weight to reduce dependence on accurate mathematical models and effectively improve parameter optimization efficiency. A mathematical model for the input stage rectifier circuit is constructed, using a traditional three-phase voltage type Pulse Width Modulation (PWM) rectifier. For ease of analysis, a switch function is defined on the Direct-Current (DC) side energy storage capacitor of the rectifier. Its operating characteristics are calculated, as shown in equation (1) [16].

$$C_1 \frac{du_{dc1}}{dt} = \sum_{k=a}^{C} i_k S_k - i_{in-DAB} = i_{dc} - i_{in-DAB} \tag{1}$$

In equation (1), where symbol C_1 represents the capacitance value of the DC side energy storage capacitor. Where symbol u_{dc1} represents the voltage across the capacitor. Where symbol i_k represents the three-phase current on the Alternating Current (AC) side. Where symbol S_k represents the three-phase switching function. Where symbol i_{in-DAB} represents the current input to the DAB converter. Where symbol i_{dc} represents the total current on the DC side. To design electronic power equipment control systems, Park transform decoupling state variables are introduced. The coordinate transformation is shown in equation (2).

$$\begin{bmatrix} X_d \\ X_q \end{bmatrix} = \begin{bmatrix} \cos\omega t & \sin\omega t \\ -\sin\omega t & \cos\omega t \end{bmatrix} \begin{bmatrix} X_\alpha \\ X_\beta \end{bmatrix} = T_{\alpha\beta\to dq} \begin{bmatrix} X_\alpha \\ X_\beta \end{bmatrix} \tag{2}$$

In equation (2), where symbol X_d and X_q represents the components of the d and q axes in a rotating coordinate system. Where symbol X_α and X_β represents two orthogonal components in a stationary coordinate system. Where symbol $T_{\alpha\beta\to dq}$ represents the transformation matrix from the $\alpha\beta$ coordinate system to the dq. After converting the coordinates, the three-phase PWM rectifier model is obtained, and the model expression is shown in equation (3) [17].

$$\begin{cases} L\dfrac{di_d}{dt} = e_d - Ri_d - u_{dc}S_d + \omega Li_q \\ L\dfrac{di_q}{dt} = e_q - Ri_q - u_{dc}S_q + \omega Li_d \\ C\dfrac{du_{dc}}{dt} = i_d S_d + i_q S_q - \dfrac{u_{dc}}{R_L} \end{cases} \tag{3}$$

In equation (3), where symbol L represents the AC side inductance. Where symbol i_d represents the current component of the d-axis. Where symbol e_d represents the d-axis component of the grid voltage. Where symbol R represents the equivalent resistance on the AC side. Where symbol u_{dc} represents the capacitor voltage on the DC side, and symbol C represents the energy storage capacitor on this side. Where symbol S_d represents the switch function of the d-axis. Where symbol R_L represents the load resistance. Afterwards, in response to the dependence of controller parameters in electronic devices on engineering experience and the long optimization time, the IIW-PSO is used to optimize controller parameters. Fig. 1 displays the PSO.

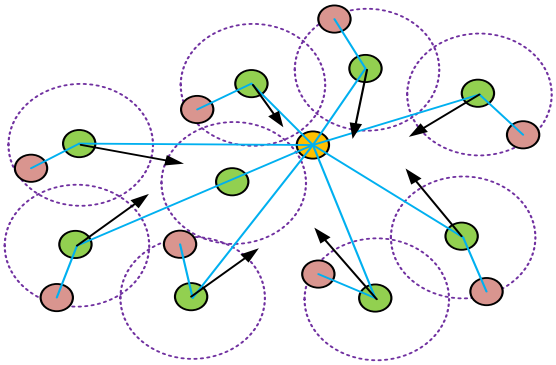

Fig. 1 PSO demonstration

In Fig. 1, the PSO originates from the bird hunting behavior. By initializing the velocity and position of the particle swarm, the fitness value is calculated. After obtaining the individual optimal solution and the global optimal solution, the velocity and position are updated. Finally, the iterative optimization reaches the termination condition and ends. The algorithm first assumes a population of N particles in a Z-dimensional space, and the position of the i-th particle is displayed in equation (4).

$$P_i = (p_{i1}, p_{i2}, \cdots, p_{iz}), i = 1, 2, \ldots, N \tag{4}$$

In equation (4), where symbol P_i represents the position vector of the i-th particle. Where symbol z represents the quantity of dimensions in space. Where symbol N represents the total particles. To optimize the rapid tuning of controller parameters, the PSO calculates the optimal combination of controller parameters. The standard update of the PSO is dispalyed in equation (5).

$$\begin{cases} v_{id}^{t+1} = \omega v_{id}^{t} + c_1 r_1 \left(P_{id}^{t} - x_{id}^{t} \right) + c_2 r_2 \left(G_{id}^{t} - x_{id}^{t} \right) \\ x_{id}^{t+1} = v_{id}^{t+1} + x_{id}^{t} \end{cases} \tag{5}$$

In equation (5), where symbol v_{id}^{t} represents the velocity component of i in the d-th dimension, where symbol ω represents the inertia weight, and symbol c_1

and c_2 represents the learning factors. Where symbol r_1 and r_2 represents random numbers evenly distributed within [0,1]. Where symbol P_{id}^t represents the individual historical optimal position of i in the d-th dimension. Where symbol G_{id}^t represents the global historical optimal position of the group. Where symbol x_{id}^t represents the current position of i. To avoid the algorithm only deriving local optima, a linear decreasing inertia weight strategy is taken, as shown in equation (6) [18].

$$\omega(t) = \omega_{\max} - \frac{(\omega_{\max} - \omega_{\min})t}{T_{\max}} \tag{6}$$

In equation (6), where symbol $\omega(t)$ represents the inertia weight at the t-th iteration, where symbol $\omega_{\max}$ represents its initial maximum value, and symbol $\omega_{\min}$ represents its minimum terminal value. Where symbol $T_{\max}$ represents the initial maximum iteration. To enhance the optimization ability of PSO for controller parameters, an improved nonlinear inertia weight attenuation strategy is constructed, as shown in equation (7).

$$\begin{cases} \omega(t) = \omega_{\min} + (\omega_{\max} - \omega_{\min})\sqrt{1 - \left(\dfrac{t}{T_{\max} \div 2}\right)^2} \left(1 \le t \le \dfrac{N}{2}\right) \\ \omega(t) = \omega_{\min} + \dfrac{4(\omega_{\max} - \omega_{\min})}{5}\sqrt{1 - \left(\dfrac{t}{T_{\max}}\right)^2} \left(\dfrac{N}{2} < t \le N\right) \end{cases} \tag{7}$$

In equation (7), where symbol $\omega(t)$ represents the inertia weight at the t-th iteration. Where symbol t represents the current iteration count. Where symbol N represents the total iterations. The inertia weight transformation curve is displayed in Fig. 2.

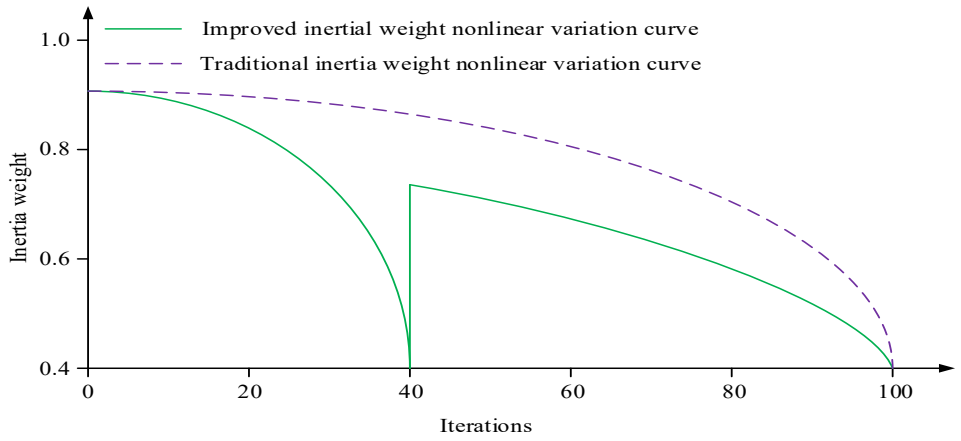

Fig. 2 Inertial weight transformation curve

In Fig. 2, the nonlinear variation curve of traditional inertia weight declines

from 0.9 to 0.4 when the iteration reaches 100. The improved non-linear curve of inertia weight gradually decreases to 0.4 after 40 iterations and then jumps out of the local optimal region design and drops back to 0.4 after 100 iterations, thereby reducing the risk of falling into local optima. Afterwards, the fluctuation of the system output is reduced. The Integral of Time Absolute Error (ITAE) serves as the fitness function for inertia weight particles. The fitness function of the i-th particle is presented in equation (8).

$$fitness = \int_0^{\infty} |e(t)|tdt \tag{8}$$

In equation (8), where symbol $fitness$ represents the fitness value. Where symbol $e(t)$ represents the error function. Where symbol t represents a time variable. The process of optimizing controller parameters based on IIW-PSO algorithm is shown in Fig. 3.

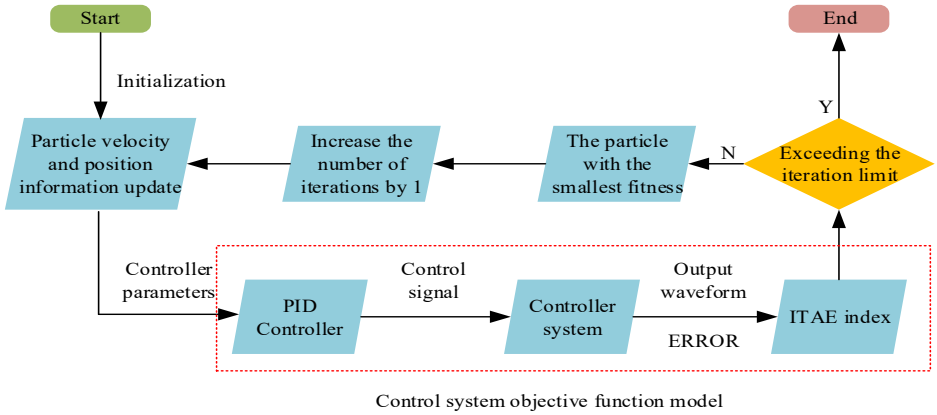

Fig. 3 Controller parameter optimization process

In Fig. 3, the particle velocity and iteration times are initialized and updated, and the controller parameters are input into the objective function model of the control system to obtain the ITAE index. Whether the global optimal fitness value converges or has the maximum teration is judged. If not reached, the optimal particle is replaced with the particle with the minimum fitness. Afterwards, the particle velocity and position are iteratively updated again, and the controller parameters are optimized.

2.2 Design of control strategy optimization method based on active damping compensation

After completing the parameter optimization of power electronic equipment controller based on IIW-PSO, to improve the stability of the equipment, the IIW-PSO is combined with various converters to optimize the control strategy, and active damping compensation is introduced to optimize the robustness and dynamic adaptability. To address the complex control in Dual active bridge (DAB) controller, an IIW-PSO algorithm is added to optimize the phase shift control strategy. The

isolated DAB converter generally has six working waveform diagrams during power forward transmission, as shown in Fig. 4.

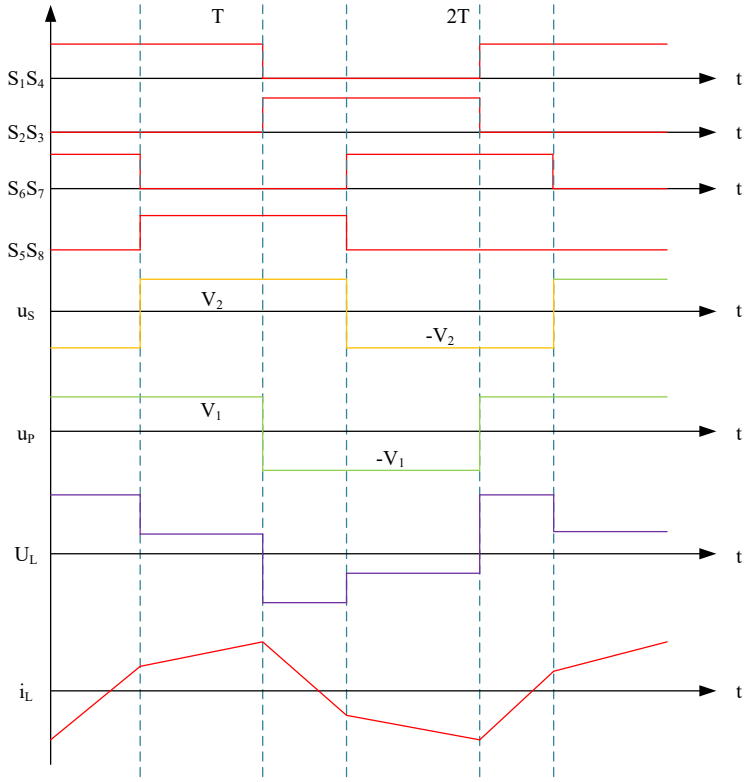

Fig. 4 Typical working waveform of DAB converter

In Fig. 4, the DAB converter has six switching modes within one switching cycle. By controlling the phase difference between the primary and secondary bridge arms, and adjusting the transmission power magnitude and direction, six modes alternate in cycles to achieve efficient energy transfer and soft switching characteristics. The voltage for the leakage inductance L_1 at both ends of mode 1 is shown in equation (9).

$$L_1 \frac{di_L}{dt} = u_{dc1} + u_{dc2} \div n \tag{9}$$

In equation (9), where symbol L_1 represents the equivalent inductance of the converter. Where symbol i_L represents the inductor current. Where symbol u_{dc1} represents the input side DC voltage. Where symbol u_{dc2} represents the output side DC voltage. Where symbol n represents the transformation ratio of the high-frequency transformer. The voltage and current of the six modes and the main circuit topology diagram is shown in equation (10).

$$\begin{cases} C_2 \dfrac{dU_{dc2}}{dt} = i_{out-\mathrm{DAB}} - i_{in-INV} \\ L_1 \dfrac{di_{L1}}{dt} = U_{dc1} - U_{dc2} n \end{cases} \tag{10}$$

In equation (10), where symbol C_2 represents the output side DC capacitor. Where symbol U_{dc1} represents the input side capacitor voltage, where symbol U_{dc2} represents the output side capacitor voltage. Where symbol $i_{out-\mathrm{DAB}}$ represents the output current of the converter. Where symbol i_{in-INV} represents the input current of the inverter. After averaging the output current, equation (11) is obtained.

$$\begin{cases} I_{in-\mathrm{DAB}} = \dfrac{P_{out-DAB}}{U_{dc1}} = \dfrac{U_{dc2} D(1-D)}{2nf_s L_1} \\ I_{out-\mathrm{DAB}} = \dfrac{P_{out-DAB}}{U_{dc2}} = \dfrac{U_{dc1} D(1-D)}{2nf_s L_1} \end{cases} \tag{11}$$

In equation (11), where symbol $I_{in-\mathrm{DAB}}$ represents the input current of the converter, and symbol $P_{out-DAB}$ represents its output power. Where symbol D represents the phase shift ratio of phase shift control. Where symbol f_s represents the switching frequency. Afterwards, the inverter link is optimized. In response to the PWM rectifiers lacking current feedback and slow dynamic response, a dual loop control strategy combining voltage outer loop and current inner loop is built. The dual loop control structure diagram of the rectifier link is shown in Fig. 5.

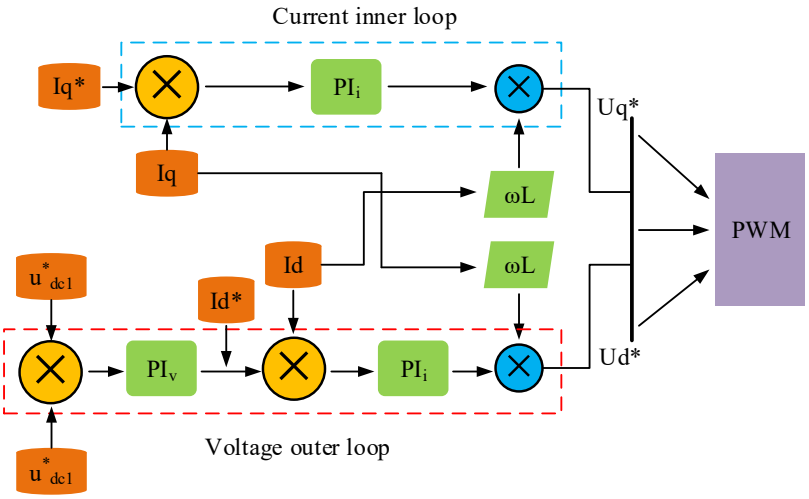

Fig. 5 Dual loop control structure diagram of rectifier link

In Fig. 5, a current inner loop is constructed, and the actual values of active and reactive currents are obtained through coordinate transformation. The current error is calculated and the tracking control is achieved. The voltage outer loop is constructed. The measured value of the DC bus voltage is input, the voltage error

is calculated, and the reference value of the current inner loop is generated through a proportional integral regulator to ensure the stability. By combining the voltage reference signal and the grid phase synchronization signal, a PWM drive signal is generated. Finally, a simplified rectifier dual loop control structure is obtained. The controller expression of the voltage current control is presented in equation (12).

$$\begin{cases} G_i(s) = -K_{pi} - K_{ii} \div s \\ G_v(s) = K_{pV} + K_{iV} \div s \end{cases} \tag{12}$$

In equation (12), where symbol $G_i(s)$ represents the controller transfer function of the current loop, where symbol K_{pi} represents its proportional gain, and symbol K_{ii} represents its integral gain. Where symbol $G_v(s)$ represents the transfer function of the voltage loop controller. Where symbol K_{pV} represents the proportional gain of the voltage loop, and symbol K_{iV} represents its integral gain. Afterwards, the output stage inverter circuit is constructed, as presented in equation (13) [19].

$$Q - Q_0 = -K_Q(e_d * - e_0) \tag{13}$$

In equation (13), where symbol Q represents the actual reactive power. Where symbol Q_0 represents the reference reactive power. Where symbol K_Q represents for adjusting the gain. Where symbol e_d* represents the dynamically adjusted target voltage. Where symbol e_0 represents the reference voltage. The active power-frequency control strategy is shown in equation (14).

$$\frac{\omega_0 - \omega}{P_0 - P_e} = \frac{1}{T_J \omega_0 s + D\omega_0 + K_p} \tag{14}$$

In equation (14), where symbol ω_0 represents the rated angular frequency. Where symbol ω represents the actual system angular frequency. Where symbol P_0 represents the reference value for active power. Where symbol P_e represents the actual output active power. Where symbol T_J represents the inertia time constant. Where symbol D represents the damping coefficient. Where symbol K_p represents the proportional adjustment gain. Where symbol s represents the Laplacian operator. The active damping compensation link is shown in equation (15)[20].

$$G_r(s) = \frac{2K_r D_r \omega_c s}{s^2 + 2\omega_c s + \omega_0^2} \tag{15}$$

In equation (15), where symbol $G_r(s)$ represents the transfer function of the active damping compensator. Where symbol K_r represents the compensation gain. Where symbol D_r represents the damping coefficient. Where symbol ω_c represents the design frequency of the compensator. Where symbol ω_0 represents the natural frequency. The inverter control strategy based on active damping compensation is shown in Fig. 6.

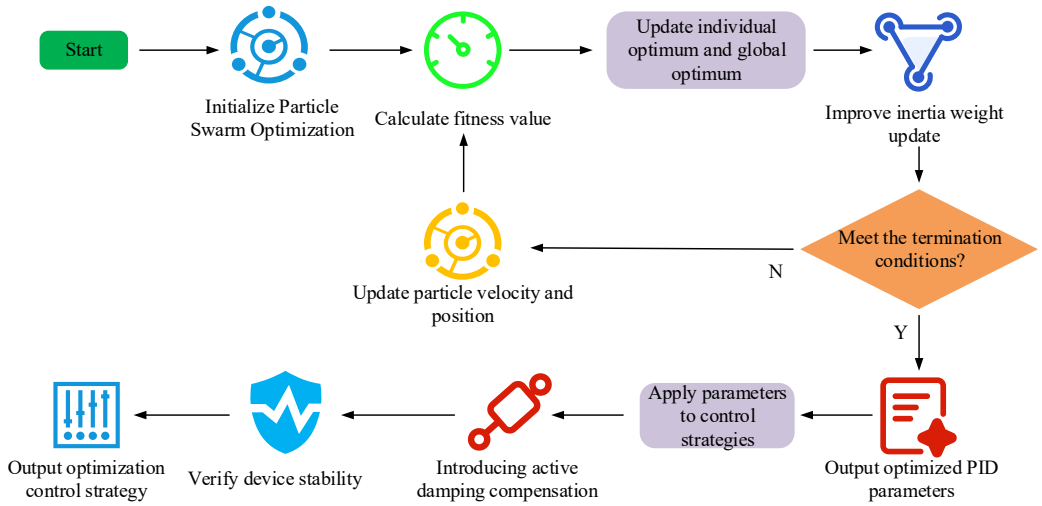

Fig. 6 Optimization process of power electronic equipment

In Fig. 6, after initializing the particle swarm, the ITAE index is calculated and the historical and global optimal positions of each particle are recorded. The nonlinear inertia weight formula updates the improved inertia weight and makes termination condition judgments. After reaching the conditions, the optimized parameters are output and applied to the control strategy of power electronic equipment. Afterwards, active damping compensation is introduced to verify the stability and output the optimized control strategy. If the conditions are not met, the particle velocity and position are updated, and the fitness value is calculated again.

3 Results

3.1 Performance testing of power electronic equipment

To assess the performance of power electronic devices based on IIW-PSO, this study compares the IIW-PSO, GA, and Grey Wolf Optimizer (GWO) algorithms. Simulink is used as the power electronics simulation software to build the equipment model, and load simulation equipment is used as the experimental platform. The parameter settings of each component of the electronic equipment system are presented in Table 1.

Table 1

The preset parameters of each component in the device

Parameter settings	Numerical value	Unit
AC side filtering inductor in rectification process	8	mH
AC side parasitic resistance in the rectification process	0.2	Ω
Rated voltage of DC bus	800	V

DAB high-frequency transformer leakage inductance	25	μH
DAB switching frequency	20	kHz
Inverter filtering capacitor	0.05	F
Inverter efficiency	98.5	%
Overcurrent protection threshold	120	A

Based on the above system component parameter settings, this study measures the algorithm convergence performance and power quality of the equipment through indicators such as voltage tracking error, power loss, and Total Harmonic Distortion (THDR) for three methods. Firstly, the voltage tracking error and power loss are compared as shown in Fig. 7.

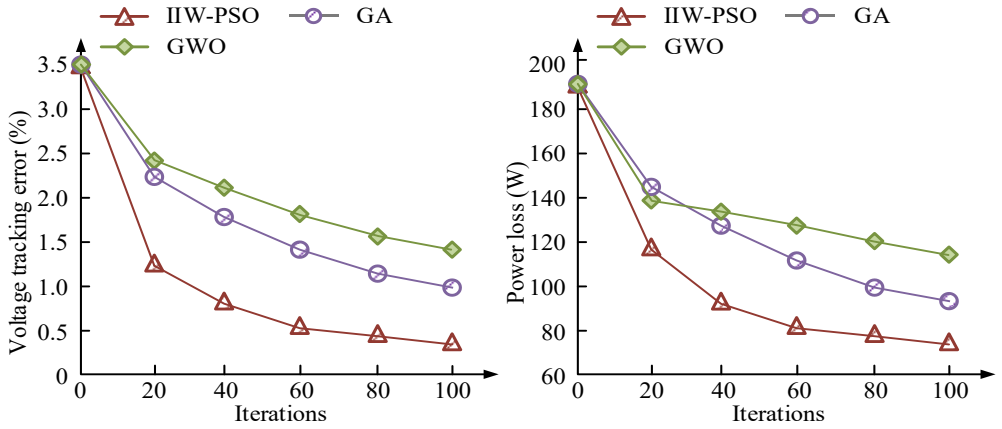

(a) Voltage tracking error rate test (b) Power loss test

Fig. 7 Comparison of voltage tracking error and power loss

As shown in Fig. 7, the convergence trend of the algorithm was consistent among different methods during the iterative optimization process. As shown in Fig. 7 (a), the IIW-PSO algorithm experienced a sharp decline in the first 20 iterations, with the voltage tracking error rate dropping to 1.25%. The change showed a rapid decline, gradually slowing down in the latter, until the error rate was only 0.4% at the end of the iteration. The overall error values were lower than those of the GA and GWO algorithm. According to Fig. 7 (b), in the first 20 iterations, the convergence speed of IIW-PSO was faster than GA and GWO algorithm, and the power loss decreased to 75W when the number of iterations reached 100. GWO algorithm had a faster descent speed than GA in the first 20 iterations, but the descent speed slowed down and was lower than GA afterwards. Overall, the IIW-PSO has better convergence performance and higher computational efficiency. Afterwards, to test the power quality, three methods are compared using the THDR

as an indicator, as shown in Fig. 8.

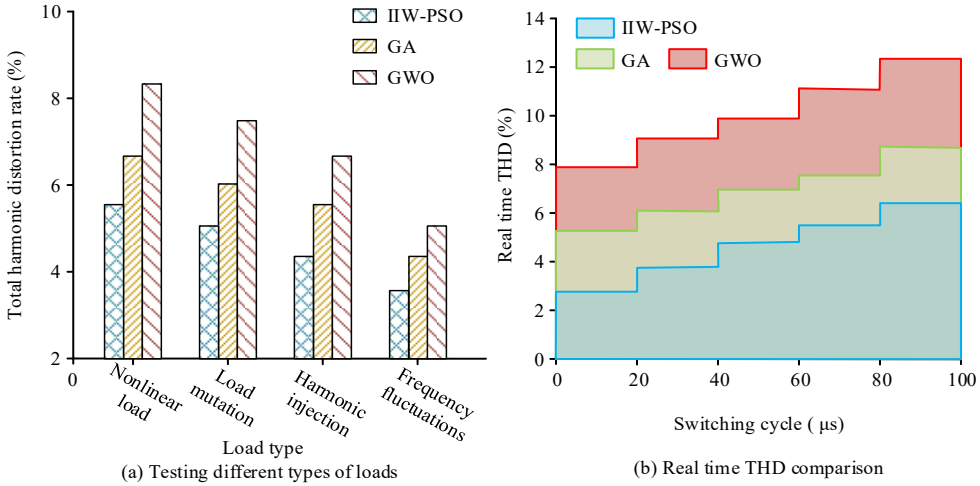

Fig. 8 Comparison of total harmonic distortion

Fig. 8 (a) displays the THD test results for different types of disturbances, and Fig. 8 (b) displays the real-time THD test results for different switching periods. According to Fig. 8 (a), the IIW-PSO algorithm had a THD of 5.7% under nonlinear loads, which was much lower than the 6.8% of GA and the 8.4% of GWO. When the disturbance type was frequency fluctuation, the maximum THD of GWO was 5.1%, while the THD of IIW-PSO was only 3.3%. Its overall THD was below that of GWO algorithm and GA. In Fig. 8 (b), the real-time THD of the IIW-PSO was linearly related to the size of the switching period. As the switching period increased, the real-time THD of the IIW-PSO also increased, reaching 5.8% at a switching period of 100 μs. The real-time THD of GA was also linearly related to the switching period, but the overall distortion rate was higher than that of IIW-PSO. The real-time THD of GWO algorithm was higher than that of GA and IIW-PSO algorithm, reaching a maximum of 12.1%. Overall, the IIW-PSO algorithm has lower THD than the GA and GWO algorithm under different types of disturbances and switching periods, indicating that the research method has higher power quality and anti-interference performance.

3.2 Simulation testing of power electronic equipment

To further verify the stability performance of power electronic devices based on IIW-PSO in practical applications, the study uses the benchmark model of the International Conference on Power Grids as the source of stability testing data. Approximately 8GB of simulation data packages released in 2020 are used as test data. To test the voltage stability under various external interferences, the output voltage of power electronic devices is used as an indicator to record the voltage waveform output to the device grid side, as shown in Fig. 9.

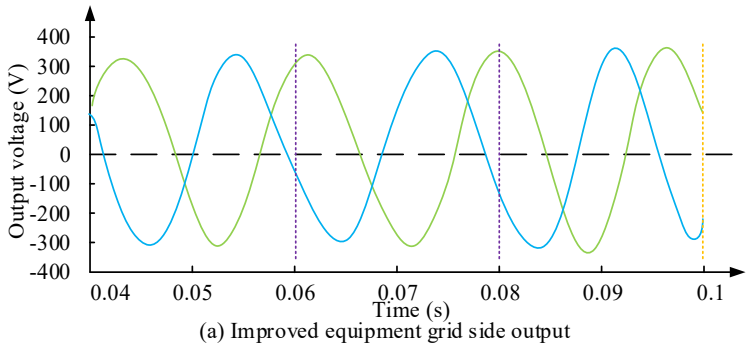

(a) Improved equipment grid side output voltage waveform

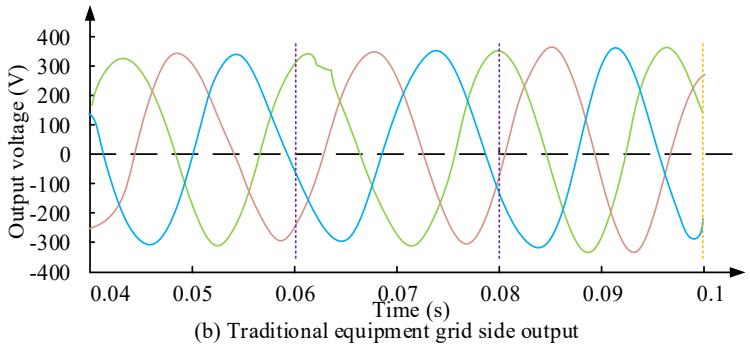

(b) Traditional equipment grid side output voltage waveform

Fig. 9 Comparison of total harmonic distortion rate

Fig. 9 (a) shows the grid side output voltage waveform of power electronic devices based on IIW-PSO, while Fig. 9 (b) shows the grid side output voltage waveform of traditional power electronic devices. During the input voltage process, at 0.06s, the voltage of the DAB converter was increased to 110% of its original value. According to Fig. 9 (a), at 0.062s, there was no significant distortion in the output voltage, and the voltage value reached 307.6V. At 0.08s, the voltage reached 316.5V, with a sudden change of 8.9V, which was 2.9% of the steady-state voltage (311V). According to Fig. 9 (b), at 0.063s, the output voltage of traditional equipment showed significant distortion. The sampled voltage value at this point was 336.2V, and it reached steady-state after 0.02s. At 0.08s after reaching steady-state, the voltage reached 312.9V. The voltage surge reached 7.5% of the steady-state value (311V). The results indicate that power electronic devices based on IIW-PSO have stronger anti-interference ability against input voltage. Further research is conducted to test the robustness of improved power electronic equipment. The steady-state error and steady-state voltage error are compared, as shown in Fig. 10.

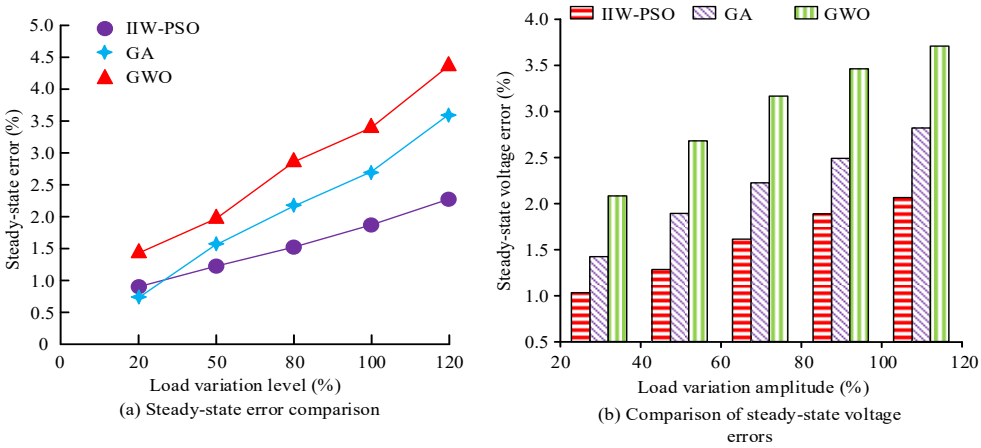

Fig. 10 Comparison of steady-state error and steady-state voltage error percentage

Fig. 10 (a) displays the steady-state error test results, and Fig. 10 (b) shows the steady-state voltage error test results. In Fig. 10 (a), the steady-state error of the IIW-PSO algorithm was linearly related to the load variation. As the load level increased, the steady-state error also increased. When the load level reached 120%, the error reached 2.1%. The steady-state error of GA was slightly lower than that of IIW-PSO algorithm at a load level of 20%, only 0.7%. Its steady-state error grew faster than the IIW-PSO algorithm, ultimately reaching 3.4%. From Fig. 10 (b), the steady-state voltage error of the IIW-PSO was also linearly related to the load variation amplitude. When the load variation amplitude was 20%-40%, the steady-state voltage error reached 1.0%. When the load variation amplitude was between 100% and 120%, the steady-state voltage error was only 1.9%. The overall steady-state voltage error of this method was lower than that of GA and GWO. Yhe research method has higher robustness. The anti-interference performance of improved power electronic equipment is tested, taking output voltage and input voltage as indicators, as shown in Fig. 11.

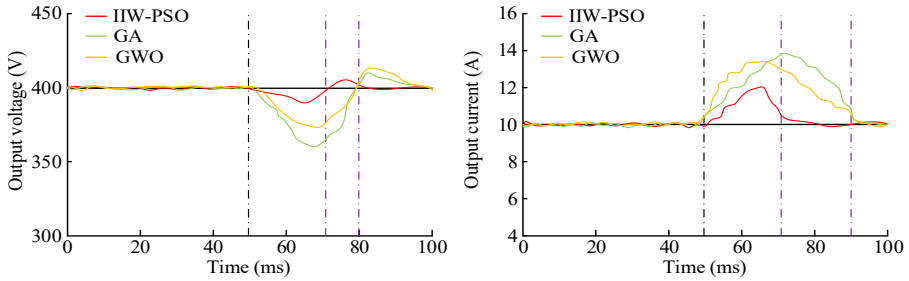

Fig. 11 Comparison of steady-state error and steady-state voltage error percentage

Fig. 11 (a) displays the output voltage test results, and Fig. 11 (b) displays the output current test results. In Fig. 11 (a), when interference was applied to the

voltage at 50ms, the voltage of the IIW-PSO algorithm dropped to 391V, reached 407V at 74ms, and stabilized at 400V at 100ms. The GA decreased to 364V at 68ms, reached a maximum voltage of 419V after 17ms, and finally stabilized at 400V. As shown in Fig. 11 (b), when interference was applied to the output current at 50ms, the IIW-PSO algorithm reached a peak current of 12.1A after 16ms and stabilized at 10A at 83ms. The GWO algorithm reached the peak current earlier than the IIW-PSO, but the peak current reached 13.8A and stabilized at 10A at 92ms. In summary, the voltage and current changes of the IIW-PSO are below those of the GA and GWO, proving that the research method has higher dynamic anti-interference performance and can enhance the stability of power electronic equipment.

4. Conclusion

Aiming at the problem that the controller parameters based on traditional stability optimization methods for power electronic equipment rely too much on engineering experience and have a long optimization time, an innovative stability optimization method based on IIW-PSO was built. This method optimized the controller parameters by improving the inertia weight PSO and introduced active damping compensation to adjust the damping strength in real time. The control strategies of each converter in the equipment are optimized. The power loss of the research method was 75W after 100 iterations, and the highest real-time THD was only 5.8%, indicating that the improved equipment had higher convergence ability and power quality. In practical application, its voltage surge was 2.9%, much lower than the 7.5% of traditional equipment. The maximum steady-state voltage error was only 1.9%, and the peak current reached 12.1A at 66ms, verifying that this method had higher robustness and voltage anti-interference ability. Overall, the stability optimization method for power electronic equipment based on IIW-PSO has excellent controller parameter optimization capabilities and can effectively improve the stability of control strategies for various converters. Its performance can meet the stability requirements of power electronic equipment. Although the IIW-PSO has shown advantages in optimizing the stability of power electronic equipment, it has only optimized the controller parameters under low dimensional conditions. Its ability to optimize controller parameters under high-dimensional conditions still needs to be explored. In the future, improvements will be made in more fields, continuously improving the universality of the research method and the efficiency of parameter optimization.

REFERENCE

[1] *Mohammadi E, Alizadeh M, Asgarimoghaddam M Wang X, Simões M. G.* A review on application of artificial intelligence techniques in microgrids. IEEE Journal of Emerging and Selected Topics in Industrial Electronics, 2022, 3(4): 878-890.

[2] *Zheng L, Marellapudi A, Chowdhury V R, Bilakanti N, Kandula R P, Saeedifard M, et al.* Solid-state transformer and hybrid transformer with integrated energy storage in active distribution grids: Technical and economic comparison, dispatch, and control. IEEE Journal of Emerging and Selected Topics in Power Electronics, 2022, 10(4): 3771-3787.
[3] *Zhang D, Chen M, Li B, Wang X, Sun X, Jiang F.* Synchronization strategy based on resonant current detection for bidirectional wireless charging system. IEEE Transactions on Power Electronics, 2022, 37(9): 11436-11449.
[4] *Hu Q, Han R, Quan X, Wu Z, Tang C, Li W, et al.* Grid-forming inverter enabled virtual power plants with inertia support capability. IEEE Transactions on Smart Grid, 2022, 13(5): 4134-4143.
[5] *Li Y, Yan J.* Cybersecurity of smart inverters in the smart grid: A survey. IEEE Transactions on Power Electronics, 2022, 38(2): 2364-2383.
[6] *Ma K, Xia S, Qi Y, Cai X, Song Y, Blaabjerg Fl.* Power-electronics-based mission profile emulation and test for electric machine drive system—Concepts, features, and challenges. IEEE Transactions on Power Electronics, 2022, 37(7): 8526-8542.
[7] *Lyu H, He J, Li B, Jin Y.* Review on fault current limiting equipment in flexible DC distribution system. IET Conference Proceedings CP899. Stevenage, UK: The Institution of Engineering and Technology, 2024, 2024(25): 28-33.
[8] *Sun P, Xu H, Yao J, Chi Y, Huang S, Cao J.* Dynamic interaction analysis and damping control strategy of hybrid system with grid-forming and grid-following control modes. IEEE Transactions on Energy Conversion, 2023, 38(3): 1639-1649.
[9] *Rivera S, Goetz S M, Kouro S,Lehn, P W, Pathmanathan M, Bauer P, et al.* Charging infrastructure and grid integration for electromobility. Proceedings of the IEEE, 2022, 111(4): 371-396.
[10] *Meng X, Jia Y, Xu Q, Ren C, Han X, Wang P.* A novel intelligent nonlinear controller for dual active bridge converter with constant power loads. IEEE Transactions on Industrial Electronics, 2022, 70(3): 2887-2896.
[11] *Pirozmand P, Jalalinejad H, Hosseinabadi A A R, Mirkamali S, Li Y.* An improved particle swarm optimization algorithm for task scheduling in cloud computing. Journal of Ambient Intelligence and Humanized Computing, 2023, 14(4): 4313-4327.
[12] *Otair M, Ibrahim O T, Abualigah L, Altalhi M, Sumari P.* An enhanced grey wolf optimizer based particle swarm optimizer for intrusion detection system in wireless sensor networks. Wireless Networks, 2022, 28(2): 721-744.
[13] *Zhang W, Zhang W.* An efficient UAV localization technique based on particle swarm optimization. IEEE Transactions on Vehicular Technology, 2022, 71(9): 9544-9557.
[14] *Tian J, Hou M, Bian H, Li J.* Variable surrogate model-based particle swarm optimization for high-dimensional expensive problems. Complex & Intelligent Systems, 2023, 9(4): 3887-3935.
[15] *Lei Z, Gao S, Zhang Z, Yang H, Li H.* A chaotic local search-based particle swarm optimizer for large-scale complex wind farm layout optimization. IEEE/CAA Journal of Automatica Sinica, 2023, 10(5): 1168-1180.
[16] *Bi K, Lv H, Chen L, Li J, Zhu Y, Huang W, et al.* A model predictive controlled bidirectional four quadrant flying capacitor DC/DC converter applied in energy storage system. IEEE Transactions on Power Electronics, 2022, 37(7): 7705-7717.
[17] *Fu C, Zhang C, Zhang G, Su Q.* Finite-time adaptive fuzzy control for three-phase PWM rectifiers with improved output performance. IEEE Transactions on Circuits and Systems II: Express Briefs, 2023, 70(8): 3044-3048.
[18] *Sun S, Yang A, Chang C, Hua G, Ren J, Lei Z, et al.* Improved multiobjective particle swarm optimization integrating mutation and changing inertia weight strategy for optimal design of

the extractive single and double dividing wall column. Industrial & Engineering Chemistry Research, 2023, 62(43): 17923-17936.

[19] *Yang S, Zheng P, Sui Y, Tong C, Wang M.* Open-circuit fault-tolerant control for pentagon winding connected five-phase current-source inverter based PMSM drives. IEEE Transactions on Industrial Electronics, 2023, 71(3): 2277-2288.

[20] *Li Y, Gao J, Zhang Z, Wang Q.* Model-Based and Model-Free Predictive Active Damping for LCL-Type Active-Front-End Rectifiers. IEEE Transactions on Industrial Electronics, 2024, 71(10): 11754-11765.